# Dual band dual focus optical coherence tomography for imaging the whole eye segment

**Shanhui Fan,[1] Lin Li,[1] Qian Li,[1] Cuixia Dai,[1] Qiushi Ren,[2] Shuliang Jiao,[3,4] and Chuanqing Zhou[1,*]**

[1] *School of Biomedical Engineering, Shanghai Jiao Tong University, Shanghai, 200240, China*
[2] *Department of Biomedical Engineering, College of Engineering, Peking University, Beijing, 100871, China*
[3] *Department of Biomedical Engineering, Florida International University, Miami, FL, 33174, USA*
[4] *shjiao@fiu.edu*
*\* zhoucq@sjtu.edu.cn*

**Abstract:** We developed an improved dual band dual focus spectral domain optical coherence tomography (SD-OCT) for *in vivo* 2D/3D imaging of the whole eye segment, including the whole anterior segment and retina. The system featured two OCT channels with two different bands centered at 840 nm and 1050 nm, which were designed to image the retina and the anterior segments of the eye, respectively. By combing the two probe light beams for co-axial scanning and separating them for focusing at different segments of the eye with a combination of three dichroic mirrors, we not only minimized the loss of the backscattered light from the sample but also improved the imaging depth, scan range and resolution. The full resolved complex (FRC) method was applied to double the imaging depth for the whole anterior segment imaging, with which an imaging depth of 36.71 mm in air was achieved. We demonstrated that this system was capable of measuring the dynamic changes of ocular dimensions, including the asphericity of the cornea and lens, during accommodation.

©2015 Optical Society of America

**OCIS codes:** (110.4500) Optical coherence tomography; (330.7322) Visual optics, accommodation; (170.3880) Medical and biological imaging; (170.4460) Ophthalmic optics and devices; (170.4470) Ophthalmology; (170.4500) Optical coherence tomography.

## References and links

1. W. Meng, J. Butterworth, F. Malecaze, and P. Calvas, "Axial length of myopia: a review of current research," Ophthalmologica **225**(3), 127–134 (2011).
2. J. F. Koretz, P. L. Kaufman, M. W. Neider, and P. A. Goeckner, "Accommodation and presbyopia in the human eye. 1: Evaluation of in vivo measurement techniques," Appl. Opt. **28**(6), 1097–1102 (1989).
3. B. J. Kaluzny, A. Szkulmowska, M. Szkulmowski, T. Bajraszewski, A. Wawrocka, M. R. Krawczynski, A. Kowalczyk, and M. Wojtkowski, "Granular corneal dystrophy in 830-nm spectral optical coherence tomography," Cornea **27**(7), 830–832 (2008).
4. H. Ishikawa and J. S. Schuman, "Anterior segment imaging: ultrasound biomicroscopy," Ophthalmol. Clin. North Am. **17**(1), 7–20 (2004).
5. J. E. Koretz, S. A. Strenk, L. M. Strenk, and J. L. Semmlow, "Scheimpflug and high-resolution magnetic resonance imaging of the anterior segment: a comparative study," J. Opt. Soc. Am. A **21**(3), 346–354 (2004).
6. M. Restori, "Imaging the vitreous: optical coherence tomography and ultrasound imaging," Eye (Lond.) **22**(10), 1251–1256 (2008).
7. W. Drexler and J. G. Fujimoto, *Optical coherence tomography: technology and applications* (Springer, 2008).
8. G. Hausler and M. W. Lindner, "'Coherence radar' and 'spectral radar'-new tools for dermatological diagnosis," J. Biomed. Opt. **3**(1), 21–31 (1998).
9. J. Zhang, P. Wang, and Z. Chen, "Long imaging range optical coherence tomography based on a narrow line-width dual band Fourier domain mode-locked swept source," Proc. SPIE **7889**, 78892P (2011).
10. B. Baumann, M. Pircher, E. Götzinger, and C. K. Hitzenberger, "Full range complex spectral domain optical coherence tomography without additional phase shifters," Opt. Express **15**(20), 13375–13387 (2007).
11. M. Wojtkowski, A. Kowalczyk, R. Leitgeb, and A. F. Fercher, "Full range complex spectral optical coherence tomography technique in eye imaging," Opt. Lett. **27**(16), 1415–1417 (2002).
12. E. Götzinger, M. Pircher, R. Leitgeb, and C. Hitzenberger, "High speed full range complex spectral domain optical coherence tomography," Opt. Express **13**(2), 583–594 (2005).

13. A. M. Davis, M. A. Choma, and J. A. Izatt, "Heterodyne swept-source optical coherence tomography for complete complex conjugate ambiguity removal," J. Biomed. Opt. **10**(6), 064005 (2005).
14. C. Zhou, J. Wang, and S. Jiao, "Dual channel dual focus optical coherence tomography for imaging accommodation of the eye," Opt. Express **17**(11), 8947–8955 (2009).
15. C. Dai, C. Zhou, S. Fan, Z. Chen, X. Chai, Q. Ren, and S. Jiao, "Optical coherence tomography for whole eye segment imaging," Opt. Express **20**(6), 6109–6115 (2012).
16. C. Dai, S. Fan, X. Chai, Y. Li, Q. Ren, P. Xi, and C. Zhou, "Dual-channel spectral-domain optical-coherence tomography system based on 3 × 3 fiber coupler for extended imaging range," Appl. Opt. **53**(24), 5375–5379 (2014).
17. A. Tao, Y. Shao, J. Zhong, H. Jiang, M. Shen, and J. Wang, "Versatile optical coherence tomography for imaging the human eye," Biomed. Opt. Express **4**(7), 1031–1044 (2013).
18. J. Zhong, Y. Shao, A. Tao, H. Jiang, C. Liu, H. Zhang, and J. Wang, "Axial Biometry of the Entire Eye Using Ultra-Long Scan Depth Optical Coherence Tomography," Am. J. Ophthalmol. **157**(2), 412–420 (2014).
19. J. Zhong, A. Tao, Z. Xu, H. Jiang, Y. Shao, H. Zhang, C. Liu, and J. Wang, "Whole eye axial biometry during accommodation using ultra-long scan depth optical coherence tomography," Am. J. Ophthalmol. **157**(5), 1064–1069 (2014).
20. M. Ruggeri, S. R. Uhlhorn, C. De Freitas, A. Ho, F. Manns, and J.-M. Parel, "Imaging and full-length biometry of the eye during accommodation using spectral domain OCT with an optical switch," Biomed. Opt. Express **3**(7), 1506–1520 (2012).
21. H.-W. Jeong, S.-W. Lee, and B.-M. Kim, "Spectral-domain OCT with dual illumination and interlaced detection for simultaneous anterior segment and retina imaging," Opt. Express **20**(17), 19148–19159 (2012).
22. A.-H. Dhalla, D. Nankivil, T. Bustamante, A. Kuo, and J. A. Izatt, "Simultaneous swept source optical coherence tomography of the anterior segment and retina using coherence revival," Opt. Lett. **37**(11), 1883–1885 (2012).
23. I. Grulkowski, J. J. Liu, B. Potsaid, V. Jayaraman, C. D. Lu, J. Jiang, A. E. Cable, J. S. Duker, and J. G. Fujimoto, "Retinal, anterior segment and full eye imaging using ultrahigh speed swept source OCT with vertical-cavity surface emitting lasers," Biomed. Opt. Express **3**(11), 2733–2751 (2012).
24. S. Fan, Y. Sun, C. Dai, H. Zheng, Q. Ren, S. Jiao, and C. Zhou, "Accommodation-induced variations in retinal thickness measured by spectral domain optical coherence tomography," J. Biomed. Opt. **19**(9), 096012 (2014).
25. D. A. Atchison, A. Bradley, L. N. Thibos, and G. Smith, "Useful variations of the Badal optometer," Optom. Vis. Sci. **72**(4), 279–284 (1995).
26. V. Westphal, A. Rollins, S. Radhakrishnan, and J. Izatt, "Correction of geometric and refractive image distortions in optical coherence tomography applying Fermat's principle," Opt. Express **10**(9), 397–404 (2002).
27. C. Du, M. Shen, M. Li, D. Zhu, M. R. Wang, and J. Wang, "Anterior segment biometry during accommodation imaged with ultralong scan depth optical coherence tomography," Ophthalmology **119**(12), 2479–2485 (2012).
28. H. Helmholtz, "Ueber die accommodation des auges," Graefes Arch. Clin. Exp. Ophthalmol. **2**(1), 1–74 (1855).
29. M. Dubbelman, G. L. Van der Heijde, and H. A. Weeber, "Change in shape of the aging human crystalline lens with accommodation," Vision Res. **45**(1), 117–132 (2005).
30. Y. Sun, S. Fan, H. Zheng, C. Dai, Q. Ren, and C. Zhou, "Noninvasive Imaging and Measurement of Accommodation Using Dual-Channel SD-OCT," Curr. Eye Res. **39**(6), 611–619 (2014).
31. A. de Castro, J. Birkenfeld, B. Maceo, F. Manns, E. Arrieta, J.-M. Parel, and S. Marcos, "Influence of shape and gradient refractive index in the accommodative changes of spherical aberration in nonhuman primate crystalline lenses," Invest. Ophthalmol. Vis. Sci. **54**(9), 6197–6207 (2013).
32. D. A. Atchison and G. Smith, "Possible errors in determining axial length changes during accommodation with the IOLMaster," Optom. Vis. Sci. **81**(4), 283–286 (2004).
33. S. A. Read, M. J. Collins, E. C. Woodman, and S.-H. Cheong, "Axial length changes during accommodation in myopes and emmetropes," Optom. Vis. Sci. **87**(9), 656–662 (2010).

## 1. Introduction

Precise ocular imaging and biometry is critical for refractive surgery, diagnosis of eye diseases, and research on ocular growth [1–3]. Simultaneous high resolution structural imaging of the whole eye components, including the cornea, crystalline lens, iris, vitreous and retina, is particularly important for the study of physiological and pathological changes of the eye. Conventional technologies, such as ultrasound imaging, scheimpflug photography, magnetic resonant imaging (MRI), and optical coherence tomography, have been widely used for clinical ophthalmologic imaging [4–6]. Among these techniques, ultrasound imaging and MRI have great imaging depth, but their resolutions are relatively low. Additionally, ultrasound imaging needs to contact with test eye and MRI is too costly to be routinely used. Pupil dilation is required in scheimpflug photography, which disturbs the physiological state in some special applications, e.g., in accommodation research.

Optical coherence tomography (OCT), a rapidly advancing biomedical imaging modality based on low coherence interferometry (LCI), can provide non-invasive high-resolution cross-sectional imaging of biological tissues, and has become a powerful tool for ocular imaging and biometry. But due to the limitation of imaging depth, it cannot image the whole eye segment simultaneously to meet the particular requirements for ophthalmic researches and disease diagnosis. The imaging depth of a spectral-domain OCT (SD-OCT) system is limited by the finite spectral resolution of the spectrometer and the Hermitian conjugate derived from Fourier transformation of the real-valued spectral interferogram [7]. Another difficulty for long-depth imaging is the tradeoff between depth of focus and lateral resolution. To simultaneously obtain high signal strength from the cornea to retina, it needs a delivery system with large depth of focus, which will sacrifice the transverse resolution.

Although successes [8–13] have been made to extend the imaging depth of FD-OCT by improving the spectral resolution of the spectrometer (SD-OCT) [8], narrowing the line width of the swept-laser source (Swept-source OCT, SS-OCT) [9], and/or using full range complex (FRC) technology to remove the mirror image [10–13], it is still unable to realize the simultaneous imaging of the shape and dimensions of the whole eye segments. Several commercial OCT systems were able to switch between anterior segment and retina imaging modes by addition or removal of optics, but in this way, simultaneous imaging of whole eye was not realized. Recently, Zhou *et al.* proposed a dual channel dual focus SD-OCT for imaging the entire anterior segment [14]. They further improved this system for simultaneously imaging the anterior segment and retina combining with FRC method [15]. Dai *et al.* also proposed a SD-OCT based on a 3 × 3 fiber coupler with only one light source and one spectrometer for the same purpose [16]. By using a galvanometer optical scanner in the reference arm, several researchers achieved whole eye imaging and biometry during accommodation in their SD-OCT systems [17–20]. Jeong *et al.* presented a SD-OCT system that employed dual illumination with orthogonal polarization states and interlaced detection by a single spectrometer with an optical switch to realize quasi-simultaneous cornea and retina imaging [21]. Dhalla *et al.* introduced a novel coherence revival-based SS-OCT system with combined polarization and depth encoding schemes, which was capable of imaging the anterior segment and retina simultaneously [22]. Taking advantage of a vertical-cavity surface emitting lasers (VCSEL), Grulkowski *et al.* achieved ultrahigh speed SS-OCT for retinal, anterior segment, and whole eye imaging [23].

Although remarkable progresses have been made to image the anterior segment and retina simultaneously or quasi-simultaneously, they suffered from several limitations, such as the small scanning area and relatively poor quality of retina imaging. Therefore, an imaging system which could simultaneously image the whole eye segment with optimized lateral resolution, field of view and scan range will greatly benefit the ophthalmic research and clinical examination.

In our previous study [15], we developed a dual channel dual focus SD-OCT system by integrating two independent fiber-based SD-OCT systems and applying the FRC method. Although this system was successful in whole eye segment imaging, it needed to be further improved. First, as 50:50 beam splitter was used to couple the probe light beams (both were centered at 840 nm) of the two OCT channels, the backscattered light in the sample arm was attenuated at least 50% for each channel, which significantly affected the image quality. Second, only one optical delivery path was designed for both anterior segment and retinal imaging, which restricted both the scan range and resolution for retinal imaging due to the limited aperture of the iris.

To solve these problems, we presented here an improved dual channel dual focus SD-OCT with two bands centered at 840nm and 1050 nm for whole eye segment imaging. Through a special optical design of the sample arm with dichroic mirrors, we not only minimized the loss of the light signal backscattered from the sample but also extended the scanning ranges by separating the scanning paths of the 1050 nm and 840 nm light beams.

This configuration allowed both the anterior and posterior segments of the eye to be imaged simultaneously with larger scan range. It also allowed the optical design of each path to be optimized for resolution and depth-of-focus. In addition, with the off-pivot-illumination FRC method, the imaging depth of anterior segment OCT (AS-OCT) can be doubled. The system was tested in human subjects successfully.

## 2. Methods

### 2.1 Experimental system configuration and performance

A schematic of the dual band dual focus SD-OCT is shown in Fig. 1. The 840nm SD-OCT (retina-OCT) was used for retina imaging. Its performance was similar to that described in our previous paper [24]. Its calibrated axial resolution and imaging depth was 10 μm and 7.22 mm in air, respectively. The peak sensitivity close to the zero-delay plane was 98 dB with a 6 dB sensitivity roll-off at 3.5 mm depth position. The sensitivity at the maximal imaging depth was 56 dB, corresponding to a sensitivity drop of 42 dB.

For AS-OCT, a super luminescent diode (SLD) light source with a center wavelength of 1050 nm and FWHM bandwidth of 55 nm (IPSDD1003, Inphenix, USA) was used. Compared with the 840 nm wavelength band, the 1050 nm wavelength band has better penetration depth due to the reduced scattering coefficient in ocular tissues, which facilitates the imaging of the anterior segment components, especially the iridocorneal angle and the lens. The spectrometer consisted of a transmission diffraction grating with 1435 lines/mm (Wasatch Photonics, USA), an imaging lens with focal length of 150 mm, and an InGaAs line-scan camera (GL2048L-10A-ENC-STD-210, 2048 pixels, 10 μm pixel width, Sensors Unlimited Inc., USA). The spectral resolution was 0.030 nm, offering a theoretical imaging depth of 9.05 mm in air. The calibrated imaging depth was 9 mm in air. The sensitivity progressively fell off with increasing imaging depth from a peak sensitivity of 98 dB at the zero-delay plane to 50 dB at a depth of 9 mm, corresponding to a maximum sensitivity loss of 48 dB (Fig. 2(a)). The 6 dB sensitivity roll-off was at the depth position of 1 mm at the both sides of the zero-delay line. Figure 2(b) shows the point spread function (PSF) at an optical path length difference of 0.5 mm. The calibrated axial resolution was 13 μm in air. The full imaging depth of AS-OCT can be extended to 18 mm in air by applying the off-pivot-illumination FRC technique [10], which was sufficient for the whole anterior segment imaging.

To synchronize the X-Y galvanometer and line-array cameras, an analog-output board with 4 channels (PCI-6731, National Instruments, USA) was used. The two cameras were set to operate at a line rate of 24,000 A-lines per second. The interference signals captured by the cameras were transferred to a computer simultaneously for signal processing and real-time imaging. A Badal system [25] was integrated in the OCT system to compensate for ocular refractive error and induce accommodation in each eye.
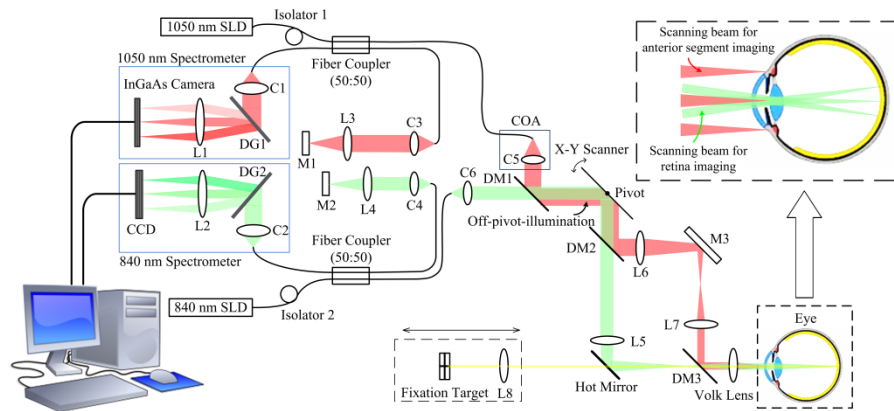
Fig. 1. Schematic of the dual band dual focus SD-OCT system. The inset is an illustration of the scanning area with dual-focus configuration. DM1-DM3: dichroic mirrors, C1-C6: collimating lenses, L1-L8: lenses, M1-M3: mirrors, COA: collimating optical assembly.
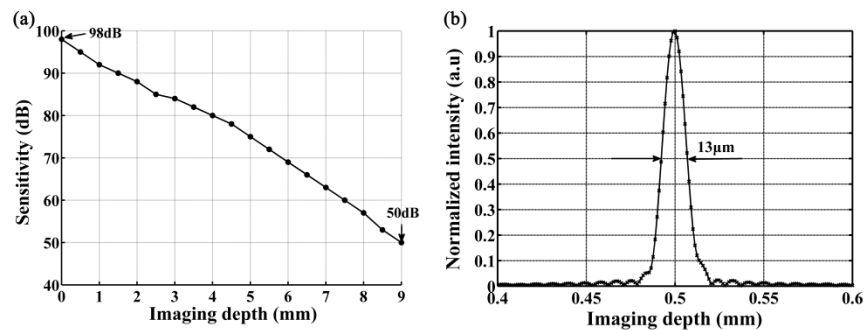


Fig. 2. The system parameters of 1050 nm SD-OCT. (a) Measured sensitivity at different imaging depths; (b) Point spread function (PSF) at an imaging depth of 0.5 mm

The total exposure power in front of the corneal surface was 2.45 mW, in which a power of 1.70 mW of the 1050 nm light beam was focused on the anterior segment and a power of 0.75mW of the 840 nm light beam was focused on the retina. We assumed the exposure time taken during imaging procedure to be longer than 10 seconds. According to the ANSI Z136.1(2007), the calculated maximum permissible exposure (MPE) for 840 light beam in this study was 44.1 mW/cm$^2$ by treating the 840 nm scanning beam as a line source, thus the corresponding maximum permissible power entering the 7-mm pupil (0.385 cm$^2$) was 16.99 mW. The quotient of applied power/safe power was 0.044 for 840 nm probe beam. The 1050 nm light beam for anterior segment imaging was convergent before cornea, so it should be seen as an extended source. Hence, the calculated MPE was 122.5 mW/cm$^2$, and the corresponding maximum permissible power entering the 7-mm pupil was 47.17 mW. The quotient of applied power/safe power was 0.036 for 1050 nm probe beam. The sum of quotients of the two light beams was 0.080, which was much smaller than 1. Therefore, according to the ANSI standard, the exposure power of probe beams applied in this study was safe for human eye.

In order to calibrate and test the system, by using a model eye (OEMI-7, Ocular Instruments Inc., USA) as a sample, we adjusted the reference arms of the two OCT subsystems to image the whole eye segments simultaneously. We first adjusted the reference arm of AS-OCT to place the zero reference plane behind the iris, which assured that the anterior segment components and their overlapping mirror image could be well visualized. Then we adjusted the reference arm of the retina-OCT to image the retina by placing the zero reference plane just behind the retina. The distance between the two reference planes was

then measured by using a mirror mounted on a translation stage as a sample. The measured distance was 11.49 mm in air. Hence, the total scan depth of this dual band SD-OCT was 36.71 mm. Knowing the distance between the images, a composite whole eye segment image from cornea to retina can be constructed in scale based on the two simultaneously acquired OCT images.

## 2.2 Sample arm optical design

The sample arm optics was specially designed to provide optimized resolution, aberration and depth-of-focus for each channel by using the combination of lenses and dichroic mirrors. As shown in Fig. 1, the light beams of 840 nm and 1050 nm were combined by a dichroic mirror (DM1) in the sample arm and scanned by X-Y galvanometer mirrors. When the scanning beams reached DM2, the 840nm beam was transmitted and collimated by lens L5 and the Volk lens, and was then focused into the retina by refractive system of the eye. After reflected by DM2, the 1050 nm light beam was guided by a mirror to DM3. Additional lenses (L6 and L7) were inserted in this path to ensure that the Volk lens can focus the 1050 nm light into the anterior segment. With this configuration, each path containing specifically designed optics was suitable for simultaneous imaging of the anterior and posterior segments of the eye. And it also offered an optimal tradeoff among the scan range, lateral resolution, and depth-of-focus for each path. The lateral resolutions of AS-OCT and retina-OCT were 61 μm and 22 μm, respectively. The simultaneous scan widths of AS-OCT and retinal-OCT were 14 mm and 10 mm, respectively. The collimating optical assembly for the 1050 nm light beam in the sample arm was mounted on an x-y-z translation stage to realize the off-pivot illumination. With this configuration, we can precisely adjust the position of the light beam hitting the fast scanning mirror to achieve a constant phase shift ($\pi/2$) between adjacent A-scans for FRC algorithm (Fig. 1). The offset of 1050 nm light beam with respect to the scanning mirror's pivot was 1.92mm.

## 2.3 Data processing

The signal processing was similar to that reported previously [15, 16]. For constructing the anterior segment image, a complex conjugate removal algorithm [10] was used to suppress the mirror image. The 2D spectral data acquired from the off-pivot configuration were Fourier transformed line by line in the transversal scanning direction. And then the result was filtered with the Heaviside step function to keep only the positive modulation frequency. Once the complex spectral data were reconstructed by inverse Fourier transform, they were interpolated to achieve linear sampling in the $k$ space. Then, the conventional SD-OCT data processing method was applied to get B-scan image with the optimal suppression of mirror image. For retina imaging, the conventional signal processing was performed without the complex conjugate removal algorithm, because the imaging depth of retina-OCT is sufficient for retina imaging. The cross-sectional image of the whole eye segment can be constructed in scale and ocular biometry can be calculated based on the optical-corrected whole eye segment image.

Ocular parameters, including the corneal thickness (CT, measured from the central corneal epithelium to the central corneal endothelium), curvature radius and eccentricity of the anterior and posterior surface of the cornea (RAC and RPC, EAC and EPC), anterior chamber depth (ACD, measured from the corneal epithelium to the anterior surface of the lens), lens thickness (LT, measured from the anterior pole to the posterior pole of the lens), curvature radius and eccentricity of anterior and posterior surface of the lens (RAL and RPL, EAL and EPL), vitreous thickness (VT, measured from the posterior surface of the lens to the internal limiting membrane [ILM]), retinal thickness (RT, measured from ILM to retinal pigment epithelium [RPE]) and axial length (AL, measured from the corneal epithelium to RPE), were calculated along the specular reflex. The boundaries of the corneal surfaces, lens surfaces, ILM and RPE layers were segmented manually. To determine the curvature radius and eccentricity, the surface was fitted with conic approach. Intraocular distance was

calculated with the division between optical path length (*OL*) and its corresponding refractive index. The refractive index of cornea, aqueous humor, lens, vitreous and retina used in this study was 1.387, 1.342, 1.415, 1.341 and 1.380, respectively. AL was defined as the sum of CT, ACD excluding the CT, LT, VT, and RT.

*2.4 Subjects*

Twelve subjects (right eye, mean spherical error: −3.0 ± 1.8 D; astigmatism < 0.5 D; 6 men and 6 women) aged from 22 to 32 years old (mean age: 28.1 ± 3.3 y) were recruited from the students of Shanghai Jiao Tong University for this study. The maximum amplitude of accommodation of each subject was larger than 6D measuring with the push-up method. All subjects had neither abnormal ophthalmological findings nor history of ocular disease, surgery, or trauma. The study was performed in accordance with the tenets of the Declaration of Helsinki. The subjects understood the nature and possible consequences of this research and signed the informed consent.

## 3. Results

The right eyes of the subjects were imaged *in vivo* to demonstrate the capability of the dual band dual focus SD-OCT system. No drug was used to stabilize the eyeball or for mydriasis. During imaging, the subject was asked to sit in front of a modified slit-lamp and fixate at the crosshair target through a Badal system (as shown in Fig. 1). The fellow eye was covered throughout the experiment to ensure reliable fixation of the test eye. The fixation target was first adjusted to the optical far point of the eye to compensate for the refractive error. OCT images were acquired when the anterior segments and retina were clearly visualized with a specular reflex. Then the operator moved the target forward to induce + 6 D accommodation. Three repeated measurements were performed in relaxed and + 6 D accommodated states during each test session. Two independent test sessions were performed for each eye with 30-minute break to test the reproducibility of the measurements.

*3.1 Simultaneous imaging of the whole eye segment*

The architecture of the anterior segment of the eye was imaged by AS-OCT. Figure 3 is the whole anterior segment images with (Fig. 3(b)) and without (Fig. 3(a)) applying the FRC algorithm. With the FRC algorithm, the complex conjugate of the OCT signal can be removed, which doubled the imaging depth of AS-OCT. As shown clearly, the mirror image in Fig. 3(a) was suppressed sufficiently in Fig. 3(b) which shows the whole anterior segment of the eye. The cross-sectional image of anterior segment clearly visualized the cornea, iris, entire lens and anterior chamber angle, and spanned the entire transverse anterior chamber width from limbus to limbus.
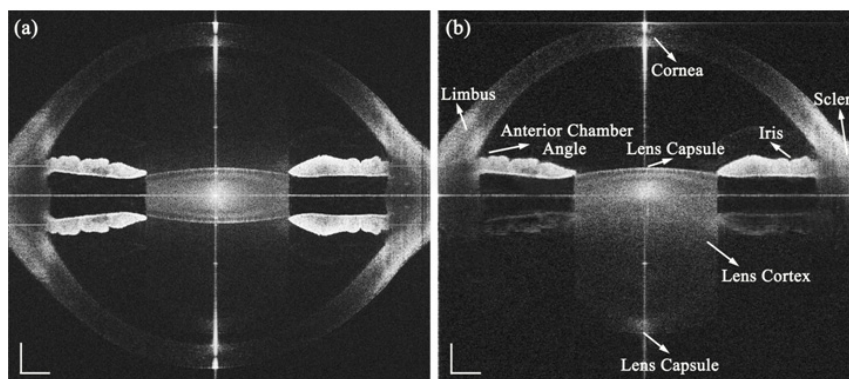
Fig. 3. Anterior segment image acquired from AS-OCT. (a) Image using conventional SD-OCT signal processing; (b) Full range reconstruction by FRC technique; Image size: 12.33 mm (depth) × 14 mm (width); 2048 A-scans/B-scan. White bar: 1 mm.

Figure 4 shows the cross-sectional image of the retina acquired from retina-OCT, in which the retinal layer structures are well distinguished. Only a part of the entire image is presented in Fig. 4(a) which has a size of 2048 (lateral) × 820 (axial) pixels. Figure 4(b) is the magnified view of the red box in Fig. 4(a), which clearly presents the major layer structures around the fovea, including the nerve fiber layer (NFL), inner plexiform layer (IPL), inner nuclear layer (INL), outer plexiform layer (OPL), outer nuclear layer (ONL), external limiting membrane (ELM), the photoreceptor inner and outer segments (IS/OS), retinal pigment epithelium (RPE), and choroid.
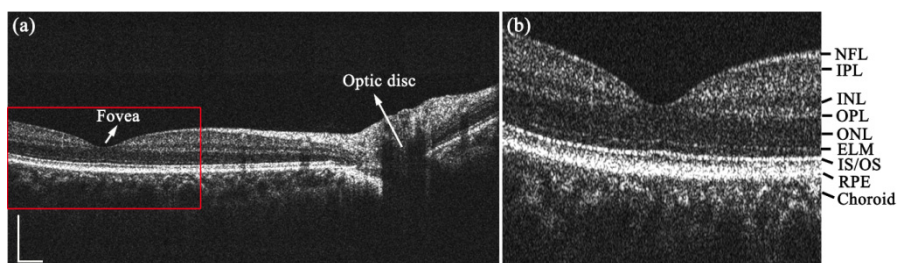


Fig. 4. Retina image acquired from retina-OCT (a) and magnification of the macular region around the fovea (red box in (a)) (b). NFL: nerve fiber layer, IPL: inner plexiform layer, INL: inner nuclear layer, OPL: outer plexiform layer, ONL: outer nuclear layer, ELM: external limiting membrane IS/OS: photoreceptor inner/outer segments, RPE: retinal pigment epithelium. White bar: 0.5 mm.

According to the imaging depths of the two images and their distance, the image of the whole eye segment can be constructed in scale (Fig. 5). Since the retinal thickness was much less than the ocular axial length, the image of retina was compressed and the details of retinal structure may not be as clear as that shown in an enlarged image (Fig. 4). Due to the distortion of the anterior segment image caused by the refraction at the curved ocular surface, a correction method similar to that in [26] must be done before the composition of the whole eye segment image and dimension calculations. Figure 5(a) shows the 3D image of the whole eye segment. The scan area of anterior segment imaging was $14 \times 14$ mm$^2$ with $512 \times 128$ (horizontal × vertical) axial scans. Due to the special optical design for the separation of OCT scanning beams in the sample arm, the scanning beam of 840 nm can be delivered to the retina without the obstruction of the iris, which resulted in a wider scan range of retina imaging ($10 \times 10$ mm$^2$). Figure 5(b) shows the composite whole eye segment cross-sectional image with optical correction. With manual segmentation on the corrected whole eye segment image, the surfaces of the cornea, lens and retina can be delineated. By using the information

of these surfaces, the ocular dimensions, including CT, ACD, LT, VT, RT, AL, RAC, EAC, RPC, EPC, RAL, EAL, RPL, and EPL, can be calculated, which validated the capability of this system for whole eye morphological measurement. In addition, the statistical results of the intra-class correlation coefficient (ICC) with a one-way random-effect model for ocular biometry between the two test sessions indicated good measurement reproducibility of the dual band SD-OCT ($p < 0.001$, ICC $> 0.8$).
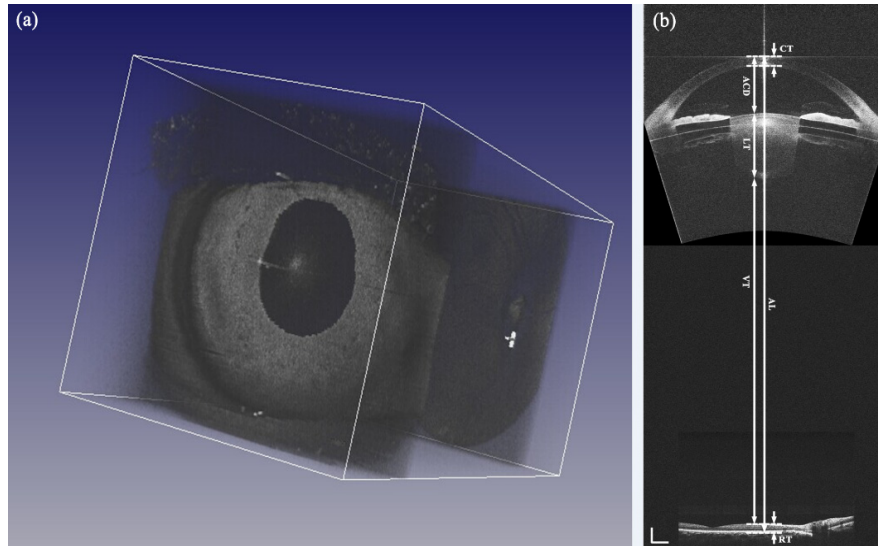


Fig. 5. Whole eye segment imaging with dual band SD-OCT in a myopic eye (−2.0 D, AL = 24.80 mm). (a) 3D reconstruction from volumetric data (Visualization 1); (b) Central cross-sectional image of the whole eye segment. CT: corneal thickness; ACD: anterior chamber depth; LT: lens thickness; VT: vitreous length; RT: retina thickness; AL: axial length. Acquisition time: 85 ms/B-scan. Image size: 36.71 mm (depth) × 14 mm (width). White bar: 1 mm.

### 3.2 Imaging and biometry of the accommodated eye

The dynamic process of the eye from relaxation to + 6 D accommodation was imaged. The changes in ocular dimensions induced by accommodation were qualitatively observed in Fig. 6 and the movie (30 y, male, −3.5 D). During accommodation, the iris became flattened and had fewer folds, both of which will result in a diminution in pupil size. In addition, the peripheral region of the anterior chamber became more capacious with the contraction of the iris sphincter muscle. Likewise, the decrease in ACD, VT, and RT, as well as the increase in LT and AL during accommodation, can also be qualitatively observed (Fig. 6).

Moreover, the quantitative changes of ocular dimensions induced by accommodation were also calculated for analysis (Table 1). The paired *t-test* was applied to assess the change of each dimension between relaxed and accommodated states in one test session. $p < 0.05$ was considered as significantly different. Compared with the relaxed state, the corneal parameters, including CT, RAC, RPC, EAC, and EPC, didn't change significantly during + 6 D accommodation ($p > 0.05$), which indicated that the cornea remained stable during accommodation; ACD, RAL, RPL, VT and RT at + 6 D accommodated state decreased significantly ($p < 0.05$), while LT and AL significantly increased during accommodation ($p < 0.05$) (Table 1). In addition, according to the analysis of Pearson correlation, significant correlations existed between the increase of LT and the decreases of ACD (r = −0.847, $p < 0.05$) or VT (r = −0.673, $p < 0.05$). However, no significant correlations between the changes of AL and ACD or LT or VT were found during accommodation ($p > 0.05$).

As the cornea was stable during accommodation, the decrease of ACD was caused by the forward movement of anterior pole of the lens which also resulted in an increase of LT. But the variation of LT was larger than that of ACD, which indicated a small backward movement of the posterior lens surface (0.106 mm) happened with a forward movement of the anterior lens surface (0.168 mm, approximately 1.6 times the backward movement) during accommodation. The backward movement of the posterior pole of the lens led to a decrease in VT. Additionally, taking the changes of LT, RAL, RPL, EAL and EPL into account, both anterior and posterior lens surfaces became more hyperbolic and curved and the lens became thicker, which also confirmed the movements and elastic deformation of lens. Due to the greater variation in RAL and EAL, the changes in anterior lens surface may play more important roles in accommodation than those did in the posterior surface. Although the variations in RPL and EPL were relatively small, the influences cannot be ignored, particular in the elders in whom the lens has a higher refractive index [27].
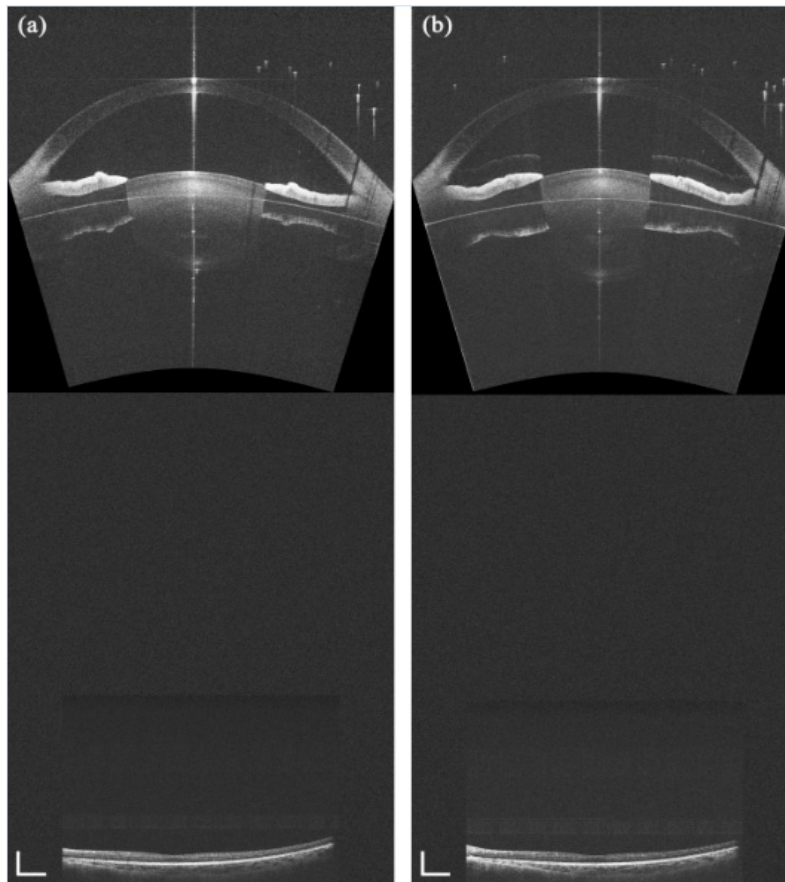


Fig. 6. Movie of OCT imaging of dynamical change in the whole eye segment from relaxed state (a) to + 6 D accommodated state (b) (Visualization 2). The frame rate of the movie is 11 fps (approximately 85 ms/frame). Image size: 36.71 mm (depth) × 14 mm (width). White bar: 1 mm.

**Table 1. The ocular biometry (mean ± standard deviation [SD]) of the whole eye at relaxed and + 6 D accommodated states**

| Ocular dimensions | Relaxed state | + 6 D accommodated state | Difference | p-value [a] |
|---|---|---|---|---|
| CT (mm) | 0.519 ± 0.026 | 0.518 ± 0.025 | −0.001 ± 0.008 | 0.565 |
| RAC (mm) | 7.417 ± 0.243 | 7.410 ± 0.228 | −0.007 ± 0.052 | 0.661 |
| RPC (mm) | 6.264 ± 0.206 | 6.254 ± 0.200 | −0.010 ± 0.064 | 0.595 |
| EAC | 0.471 ± 0.062 | 0.478 ± 0.055 | 0.007 ± 0.018 | 0.207 |
| EPC | 0.785 ± 0.055 | 0.781 ± 0.052 | −0.004 ± 0.014 | 0.331 |
| ACD (mm) | 3.646 ± 0.373 | 3.478 ± 0.365 | −0.168 ± 0.015 | < 0.001 |
| LT (mm) | 3.785 ± 0.286 | 4.059 ± 0.278 | 0.274 ± 0.021 | < 0.001 |
| RAL (mm) | 10.587 ± 0.503 | 6.399 ± 0.173 | −4.188 ± 0.460 | < 0.001 |
| RPL (mm) | −6.110 ± 0.185 | −4.872 ± 0.191 | 1.238 ± 0.234 | < 0.001 |
| EAL | 0.960 ± 0.014 | 0.987 ± 0.013 | 0.027 ± 0.006 | < 0.001 |
| EPL | 0.950 ± 0.017 | 0.955 ± 0.016 | 0.005 ± 0.003 | < 0.001 |
| VT (mm) | 16.917 ± 0.861 | 16.851 ± 0.857 | −0.066 ± 0.016 | < 0.001 |
| RT (mm) | 0.270 ± 0.041 | 0.256 ± 0.040 | −0.014 ± 0.002 | < 0.001 |
| AL (mm) | 24.600 ± 0.955 | 24.627 ± 0.954 | 0.027 ± 0.008 | < 0.001 |

CT: corneal thickness; RAC and RPC: curvature radius of anterior and posterior corneal surfaces; EAC and EPC: eccentricity of anterior and posterior corneal surfaces; ACD: anterior chamber depth; LT: lens thickness; RAL and RPL: curvature radius of anterior and posterior lens surfaces; EAL and EPL: eccentricity of anterior and posterior lens surfaces; VT: vitreous thickness; RT: retinal thickness; AL: axial length
Difference = + 6 D accommodated - Relaxed

[a]: Paired *t-test*

## 4. Discussion

In this study, we proposed a novel dual band dual focus SD-OCT, which was improved from our previous dual channel version [15], for high quality simultaneous real-time imaging of the whole anterior segment and retina *in vivo*. By using different bands and scanning paths for anterior segment and retina imaging, the new imaging system has several advantages. First, the new system employed dichroic mirrors to combine and separate the 1050 nm and 840 nm light beams in the sample arm, which solved the attenuation problem caused by a 50:50 beam splitter in our previous system [15]. Moreover, separating the two light beams into different paths also provided the optimal optical design among the scan range, lateral resolution and depth-of-focus for both retina and anterior segment imaging. With this configuration, the scan range and resolution of retina imaging will not be sacrificed as those in our previous versions [15, 16] and other reported experimental systems [17, 20, 23]. Second, since the scattering coefficient of the ocular tissues at 1050 nm was smaller than that at 840 nm, longer imaging depth and clearer anterior angle imaging was achieved. Accompanying with FRC method, the whole anterior segment, especially the whole lens, can be imaged. Finally, our imaging system can obtain a high-resolution wide-field retina image without any change in optical part of the hardware, thus it avoided the adjustments in the optical alignment and the need for dispersion compensation.

With capability of high resolution 2D/3D imaging and precise ocular biometry, this dual band imaging system is potential to be a powerful tool for studying the changes in ocular structure during accommodation. In this study, our results on the biometry of the whole eye segment during accommodation were in agreement with those of Helmholtz theory and others

[19, 20, 24, 27–30]. During accommodation, the decrease in ACD and VT and the increase in LT indicated the forward movements of the anterior lens surface and backward movements of the posterior lens surface. The changes in RAL, RPL, EAL, and EPL proved the change in the lens shape during accommodation. Taking considerations of the axial biometry, curvature radius and asphericity of the lens, the accommodation-induced deformation of the lens can be analyzed more precisely. Thus, this system was particularly useful for study on the accommodation mechanism, and consequently the origin of presbyopia and myopia.

Most of the ocular changes reported in this study could be explained by Helmholtz theory and were well documented, except for the increase of AL. To date, the explanation for the change in AL caused by accommodation is still under debate. One hypothesis is that the accommodation-induced ciliary muscle constriction causes the AL elongation, i.e., the ciliary muscle constriction generates a inward pull force towards the choroid and sclera, in order to maintain a constant ocular volume, the posterior portion of the globe displaces rearward, which results in an increase of AL. Another hypothesis is that the increase of AL is measurement artifacts caused by the change of refractive index of the lens during accommodation. de Castro *et al.* [31] found that the gradient refractive index of the lens remained constant during accommodation, which suggested that the average refractive index may not change during accommodation. With the assumption of no change in refractive index of the lens during accommodation, Atchison and Smith [32] estimated the ocular *OL* of Gullstrand accommodated schematic eyes (10.9 D) containing different types of the lens theoretically. The anatomical AL of three schematic eyes was the same. The results showed that the average overestimation of *OL* for per diopter was 1.6 μm (containing shell lens) and 2.4 μm (containing gradient lens) compared with that in Gullstrand unaccommodated schematic eye. Hence, they believed that the change of the measured AL without consideration of the change in refractive index of lens during accommodation will be overestimated. In their paper, they proposed the correction method for this overestimation. Later, Read *et al.* [33] used the similar method to correct the AL measured with LENSTAR for + 3 D and + 6 D accommodations. With the corrected results, the increase in AL with + 3 D and + 6 D accommodation stimuli was 5.2 μm and 7.4 μm, respectively. In our study, an increase of 27 μm in AL during + 6D accommodation (approximately 54.5 μm in *OL*, i.e. 9.1 μm/D) was measured under the condition that the refractive index of the lens was stable during accommodation, its magnitude was greater than the overestimation reported by Atchison and Smith [32], so the increase in AL wasn't all attributable to the existence of this overestimation in this study. Our results were also consistent with those reported by Wang [19]. For these reasons, we speculated that the axial length was elongated during accommodation, which may contribute to the further study of association between accommodation and near-work induced transient myopia (NITM).

Compared with IOLMaster or LENSTAR, our OCT system provides not only a depth profile for ocular axial biometry, but also high resolution cross-sectional imaging of the whole eye segment, which is helpful for direct observation and can be used for calculation of the curvature and eccentricity of ocular surface, pupil diameter and anterior chamber angle. Furthermore, the ocular dimensions can be obtained simultaneously from single B-scan of dual band SD-OCT while IOLMaster or LENSTAR needs multiple operations.

However, it still has some limitations in this study. As shown in the Visualization 2, the complex conjugate of some frames may not be suppressed completely. This is because any sample movement in axial direction will resulted in additional phase shift, and yet the accommodation is a dynamic process which inevitably accompanies with the eye movements. Hence, faster scanning will help to improve the efficiency of mirror image suppression. Additionally, higher scan speed will minimize the artifacts caused by eye motion which is also critical for good reproducibility, dynamic measurement and 3D reconstruction. Another limitation is the missing of part of the vitreous body. This problem can be solved by extending the penetration depth of posterior segment imaging, e.g., applying the FRC method

or using a spectrometer with finer spectral resolution, because the imaging of the vitreous body is also important for the examination of the vitreous opacity, intraocular infections, and other pathological changes about the vitreous. Although the design of spectrometers used in this study is not optimized, the subsystems of dual band SD-OCT are good enough to prove the concept of this study (i.e., to demonstrate the capability of dual band SD-OCT for whole eye segment imaging). In addition, the refractive indices used in this study may induce small calculation error.

## 5. Conclusion

In conclusion, we have demonstrated that the improved dual band dual focus SD-OCT was capable of providing the high-resolution, high-contrast 2D/3D whole anterior segment and retina imaging simultaneously as well as the precise ocular biometry. The results presented in this study also demonstrated the feasibility of applying this OCT system for imaging and measuring the dynamic changes of ocular dimensions during accommodation. Hence, the high performance of dual band SD-OCT enabled it to be a powerful imaging tool for ophthalmic diagnosis and researches, such as ocular growth, presbyopia, myopia, accommodation and other physiological and pathological changes of the eye.

## Acknowledgments